INTERNATIONAL JOURNAL FOR NUMERICAL METHODS IN FLUIDS
Int. J. Numer. Meth. Fluids 2001; **35**: 71–91

The solution of viscous incompressible jet flows using non-staggered boundary fitted co-ordinate methods

J. Rafael Pacheco*,[1]

Department of Mathematics, Arizona State University, Tempe, AZ, U.S.A.

SUMMARY

A new approach for the solution of the steady incompressible Navier–Stokes equations in a domain bounded in part by a free surface is presented. The procedure is based on the finite difference technique, with the non-staggered grid fractional step method used to solve the flow equations written in terms of primitive variables. The physical domain is transformed to a rectangle by means of a numerical mapping technique. In order to design an effective free solution scheme, we distinguish between flows dominated by surface tension and those dominated by inertia and viscosity. When the surface tension effect is insignificant we used the kinematic condition to update the surface; whereas, in the opposite case, we used the normal stress condition to obtain the free surface boundary. Results obtained with the improved boundary conditions for a plane Newtonian jet are found to compare well with the available two-dimensional numerical solutions for Reynolds numbers, up to $Re = 100$, and Capillary numbers in the range of $0 \leq Ca < 1000$. Copyright © 2001 John Wiley & Sons, Ltd.

KEY WORDS: boundary fitted method; finite difference method; jet flows

1. INTRODUCTION

The presence of one or more free surface boundaries complicates the analysis of many fluid flows of practical interest. Analytical solutions of free surface flow problems are virtually non-existent, and increasingly, numerical methods are being employed to predict local flow properties. Like the unknown pressure and velocities, the shape and the position of the boundary must be determined as part of the solution. The flow characteristics at steady state are interesting from a practical point of view. Perturbations are imposed on steady state conditions in order to study flow instabilities [1–4]. Since the die swell has a direct influence on the dimensions of the final product in processes like extrusion, fiber spinning, and blow molding, it is necessary to obtain a fundamental understanding of the die swell phenomenon in order to ensure successful design and operation of the processes.

* Correspondence to: Department of Mathematics, Arizona State University, PO Box 1804, Tempe, AZ 85287-1804, U.S.A.
[1] E-mail: rpacheco@asu.edu

Received 13 September 1999
Revised 28 February 2000

The Newtonian jet swell flow is a benchmark problem to test the accuracy and robustness of numerical techniques. The flow is steady and incompressible and it is governed by the momentum and continuity equations with the boundary conditions of no-slip at the wall and no-stress at the free surface. The inflow and outflow boundaries are taken at distances L_1, L_2, sufficiently far from the jet exit so that the flow is fully developed far upstream from the inlet plane of the free section, and uniform at the outlet plane of the jet (Figure 1).

The shapes of Newtonian jets emerging from a long die depend only on two dimensionless parameters, the Reynolds number and the Capillary number (*Re* and *Ca* respectively), when gravity is neglected. In general, the die-swell ratio *Co* decreases as Reynolds number increases. The jet expands monotonically for low *Re* and contracts monotonically at high *Re*. The limit of the *Co* for a planar jet at infinite Reynolds number without surface tension is 0.833 (Tillet [5]). Surface tension is also important; in general, it reduces either expansion or contraction of the jet.

In the past many approaches have been devised yielding successful numerical solutions of steady free surface jet flows. Depending on the boundary condition that is used to locate the boundary profile, these iterative procedures are classified as kinematic iteration, normal–stress iteration, and shear–stress iteration schemes.

Finite element methods with primitive variables have been used frequently to solve the flow, e.g., Ruschak [6], Nickell *et al.* [7]. Heretofore, most of these schemes employed low-order finite elements for the spatial discretization, while the energy and momentum equations with proper boundary conditions are solved in a coupled manner. When low-order finite elements are used, the representation of the free boundary is often inadequate and splines are sometimes introduced to evaluate more accurately geometric quantities, such as curvatures and slopes.

The spectral element formulation has been applied successfully to this flow (Ho and Rønquist [8]), wherein a fast convergence in space is achieved due to the inherent high-order spatial discretization (a characteristic of the spectral formulation).

Finite difference methods with co-ordinate transformation, e.g., Han *et al.* [9], Yiu and Liu [10], have been used to solve the jet-well when the streamfunction–vorticity formulation describes the flow equations. However, this method is limited to two-dimensional flow problems.

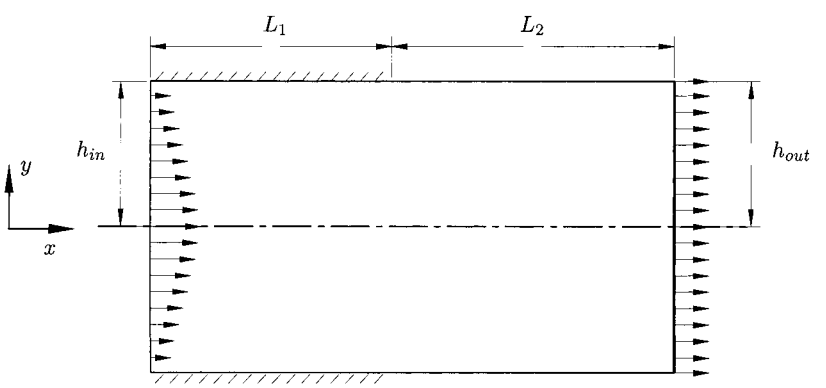

Figure 1. Slot jet flow geometry in the physical plane.

In this paper, we develop and demonstrate a technique for incorporating free boundary conditions with surface tension using primitive variables. This study follows that of Pacheco and Peck [11], but it differs in that the procedure used to locate the free surface boundary is extended and convergence is improved for both high and low Capillary numbers. The equations prescribing the free surface conditions are derived and the technique based on the non-staggered grid fractional step method given by Zang *et al.* [12] is employed to solve the equations in discretized form. The boundary fitted co-ordinate method developed by Thompson *et al.* [13] was adopted to map the flow geometry into a rectangle and a local orthogonality at the free surface was achieved by using the method described by Steger and Sorenson [14].

The numerical method is attractive because it is second-order accurate in both space and time. The accuracy is unaffected by grid orientation. Also, the method can be used to solve three-dimensional problems and unsteady flows.

The following sections contain the governing equations, the implementation of the boundary conditions, a summary of the fractional step method, and results from the different test cases.

2. GOVERNING EQUATIONS

In this study we consider viscous incompressible flow of a Newtonian fluid, with density ρ and viscosity μ in a two-dimensional domain Ω. The domain boundary Γ (Figure 1) is decomposed as $\Gamma_0 \cup \Gamma_\sigma \cup \Gamma_s \cup \Gamma_{in} \cup \Gamma_{out}$ with no-slip boundary conditions imposed on Γ_0, symmetry imposed on Γ_s, fully developed Poiseuille flow velocity on Γ_{in}, uniform velocity over the entire cross-section Γ_{out}, and traction boundary conditions imposed on Γ_σ. In the following, the physical space is denoted by $(x_1, x_2) = (x, y)$ and the computational space $(\xi_1, \xi_2) = (\xi, \eta)$.

The equations governing the flow are the Navier–Stokes and continuity equations, which are presented in the constant viscosity and constant density form. Using Einstein's convention, the governing equations are written as

$$\frac{\partial u_j}{\partial x_j} = 0 \quad \text{in } \Omega \tag{1}$$

$$\frac{\partial u_i}{\partial t} + \frac{\partial}{\partial x_j}(u_j u_i) = -\frac{1}{\rho}\frac{\partial p}{\partial x_i} + \nu \frac{\partial^2 u_i}{\partial x_j \partial x_j} + g_i \quad \text{in } \Omega \tag{2}$$

subject to the boundary conditions

$$u_i = 0 \qquad \text{in } \Gamma_0 \tag{3}$$

$$\tau_{ij} n_j = \sigma \kappa n_i + \nabla_i \sigma \quad \text{in } \Gamma_\sigma \tag{4}$$

$$\left.\begin{aligned} u &= u_{in} \\ v &= 0 \end{aligned}\right\} \quad \text{in } \Gamma_{in} \tag{5}$$

$$\left.\begin{array}{l} u = u_{\text{out}} \\ v = 0 \\ p = p_a \end{array}\right\} \quad \text{in } \Gamma_{\text{out}} \tag{6}$$

$$\left.\begin{array}{l} \dfrac{\partial u}{\partial y} = 0 \\ v = 0 \end{array}\right\} \quad \text{in } \Gamma_{\text{s}} \tag{7}$$

where $i, j = 1, 2$; u_i represents the Cartesian velocity components; p is the pressure (relative to zero ambient p_a; v is the kinematic viscosity; g_i represents the gravity components; and τ_{ij} is the stress tensor defined as

$$\tau_{ij} = -p\delta_{ij} + \mu\left(\frac{\partial u_j}{\partial x_i} + \frac{\partial u_i}{\partial x_j}\right) \tag{9}$$

where δ_{ij} is the Kronecker delta. On the free surface Γ_σ, σ is the free surface tension coefficient, n_i is the outward unit normal, ∇_i is the surface gradient operator, and κ is the curvature in two-dimensional geometry and twice the mean curvature in three-dimensional geometry. The curvature along a surface co-ordinate is considered positive if the liquid region below the free surface is concave along that surface co-ordinate.

Far downstream from the die exit, u_{out} is the uniform velocity, and at a distance far upstream, u_{in} is the velocity of the fully developed Poiseuille flow, given by

$$u_{\text{in}} = -\frac{1}{2\mu}\frac{\partial p}{\partial x}(h^2 - y^2) \tag{10}$$

where h is the height measured from the symmetry plane. Equations (1) and (2) are transformed into curvilinear co-ordinates in strong conservation law form as

$$\frac{\partial U_m}{\partial \xi_m} = 0 \tag{11}$$

$$\frac{\partial (J^{-1}u_i)}{\partial t} + \frac{\partial (U_m u_i)}{\partial \xi_m} = -\frac{\partial}{\partial \xi_m}\left(\frac{J^{-1}}{\rho}\frac{\partial \xi_m}{\partial x_i}p\right) + \frac{\partial}{\partial \xi_m}\left(vG^{mn}\frac{\partial u_i}{\partial \xi_n}\right) + J^{-1}g_i \tag{12}$$

where J^{-1} is the inverse of the Jacobian or the volume of the cell; U_m is the volume flux (contravariant velocity multiplied by J^{-1}) normal to the surface of constant ξ_m; and G^{mn} is the 'mesh skewness tensor'. These quantities are defined by

$$U_m = J^{-1}\frac{\partial \xi_m}{\partial x_j}u_j \tag{13}$$

$$J^{-1} = \det\left(\frac{\partial x_i}{\partial \xi_j}\right) \tag{14}$$

$$G^{mn} = J^{-1} \frac{\partial \xi_m}{\partial x_j} \frac{\partial \xi_n}{\partial x_j} \tag{15}$$

3. BOUNDARY CONDITIONS

As the free surface geometry deforms from an initial state, the dominant physical effect that causes this deformation needs to be identified. The three major physical forces that influence the free surface behavior are inertia, viscous, and surface tension forces. Since the surface tension contribution is directly involved in the normal traction boundary condition on the free surface, it is important to distinguish between flows dominated by surface tension from those dominated by inertia or viscosity so that we can design an effective steady state free surface solution scheme. The non-dimensional groups that indicate the relative strength of these surface forces are the Reynolds number (inertia versus viscous effects)

$$Re = \frac{\rho UL}{\mu} \tag{16}$$

where L and U are the characteristic length and velocity respectively; the capillary number (viscous versus surface tension effects)

$$Ca = \frac{\mu U}{\sigma} \tag{17}$$

and the Weber number (inertia versus surface tension effects)

$$W = \frac{\rho L U^2}{\sigma} \tag{18}$$

The correct free surface boundary conditions are the balance of the normal and tangential stress and the kinematic condition. Balancing momentum between two fluids gives

$$\tau''_{ij} n_j - \tau'_{ij} n_j = -\sigma \kappa n_i \tag{19}$$

The curvature $\kappa = 1/R_1 + 1/R_2$, where R_1 and R_2 are the radii of curvature of the orthogonal plane containing the unit normal to the surface **n**. In order to apply the appropriate boundary conditions at the free surface we have written the following identity in the chain rule conservation form:

$$J^{-1} \frac{\partial u_k}{\partial x_i} = \frac{\partial u_k}{\partial \xi_j} T^{ij} \tag{20}$$

where

$$T^{kj} = J^{-1} \frac{\partial \xi_k}{\partial x_j} \tag{21}$$

to get the derivatives for the velocities in the computational domain. For a two-dimensional surface, assuming that the external fluid (taken to be a gas here) is stress free, we can express the shear–stress balance in terms of the computational variables as

$$\frac{\partial u}{\partial \xi}(C_1 T^{12} + C_2 T^{11}) + \frac{\partial u}{\partial \eta}(C_1 T^{22} + C_2 T^{21}) + \frac{\partial v}{\partial \xi}(C_1 T^{11} - C_2 T^{12}) + \frac{\partial v}{\partial \eta}(C_1 T^{21} - C_2 T^{22}) = 0 \tag{22}$$

Similarly, the normal stress balance can be expressed in terms of the computational variables with the reference pressure $p_a = 0$ as

$$p - \left[\frac{\partial u}{\partial \xi}(C_3 T^{11} + C_4 T^{12}) + \frac{\partial u}{\partial \eta}(C_3 T^{21} + C_4 T^{22}) + \frac{\partial v}{\partial \xi}(C_4 T^{11} + C_5 T^{12}) + \frac{\partial v}{\partial \eta}(C_4 T^{21} + C_5 T^{22})\right] = -\sigma\left(\frac{1}{\bar{R}}\right) \tag{23}$$

if we let $C_1 = \mu(n_y^2 - n_x^2)J$, $C_2 = 2\mu n_x n_y J$, $C_3 = 2\mu n_x^2 J$, $C_4 = 2\mu n_x n_y J$, $C_5 = 2\mu n_y^2 J$, and $1/\bar{R} = \kappa$. Here, n_x and n_y are the components of the unit vector normal to the surface in the x- and y-directions respectively. The kinematic condition implies that there is no mass flux through the free surface; therefore, the contravariant velocity at the face of the cell is identically zero

$$V = \hat{u} T^{21} + \hat{v} T^{22} = 0 \tag{24}$$

The conditions at the inlet are of Dirichlet type and therefore do not require special manipulation. Along the line of symmetry, we can use Equation (20) to change the derivatives from the physical domain to the computational domain. At the outlet, the conditions $u = u_{\text{out}}$ and $v = 0$ are replaced by $\partial u/\partial x = 0$ and $\partial v/\partial x = 0$, and transformed to the computational domain using Equation (20).

4. DISCRETIZATION

The non-staggered grid layout is employed in this analysis. The pressure and the Cartesian velocity components are defined at the cell center and the volume fluxes are defined at the mid-point of their corresponding faces of the control volume in the computational space. We use a semi-implicit time-advancement scheme with the Adams–Bashforth method for the explicit terms and the Crank–Nicolson method for the implicit terms, as described by Zang *et al*. [12] and Pacheco and Peck [15]. Here, we will just describe how to apply numerically the boundary conditions at the free surface.

We assume that the relation between the velocity at the boundary and the velocities next to the face can be written as

$$\hat{u} = \frac{u_{i,j+1} + u_{i,j}}{2} \tag{25}$$

$$\hat{v} = \frac{v_{i,j+1} + v_{i,j}}{2} \tag{26}$$

If we consider the derivatives at the free surface are located at the center of the cell face, we can approximate the derivatives as

$$J^{-1}\frac{\partial u}{\partial x} = \frac{\delta u}{\delta \xi} T^{11} + \frac{\delta u}{\delta \eta} T^{21} \approx (\bar{u}_{i+1,j} - \bar{u}_{i,j}) T^{11}_{i,j} + (u_{i,j+1} - u_{i,j}) T^{21}_{i,j} \tag{27}$$

$$J^{-1}\frac{\partial u}{\partial y} = \frac{\delta u}{\delta \xi} T^{12} + \frac{\delta u}{\delta \eta} T^{22} \approx (\bar{u}_{i+1,j} - \bar{u}_{i,j}) T^{12}_{i,j} + (u_{i,j+1} - u_{i,j}) T^{22}_{i,j} \tag{28}$$

where the velocities with an overbar are the velocities at the corners of the cell, which have been interpolated from the velocities at the center of the cell face using a quadratic interpolation scheme (Pacheco and Peck [11]). Similar expressions can be obtained for the vertical velocity components.

In order to simplify the form of the equations that will be used for the calculation of the free surface, we define the following expressions:

$$Au_x = C_3 T^{11}_{i,j} + C_5 T^{12}_{i,j} \tag{29}$$

$$Av_x = C_4 T^{12}_{i,j} + C_5 T^{11}_{i,j} \tag{30}$$

$$Au_y = C_3 T^{21}_{i,j} + C_5 T^{22}_{i,j} \tag{31}$$

$$Av_y = C_4 T^{22}_{i,j} + C_5 T^{21}_{i,j} \tag{32}$$

and

$$Bu_x = C_1 T^{12}_{i,j} + C_2 T^{11}_{i,j} \tag{33}$$

$$Bv_x = C_1 T^{11}_{i,j} - C_2 T^{12}_{i,j} \tag{34}$$

$$Bu_y = C_1 T^{22}_{i,j} + C_2 T^{21}_{i,j} \tag{35}$$

$$Bv_y = C_1 T^{21}_{i,j} - C_2 T^{22}_{i,j} \tag{36}$$

If the normal stress balance is used to update the free surface, it can be shown that velocities outside the boundary are

$$u_{i,j+1} = \frac{[(\bar{u}_{i+1,j} - \bar{u}_{i,j})T^{22}_{i,j}Bu_x + (\bar{v}_{i+1,j} - \bar{v}_{i,j})T^{22}_{i,j}Bv_x - u_{i,j}C_1(T^{22}_{i,j}T^{22}_{i,j} + T^{21}_{i,j}T^{21}_{i,j}) - 2v_{i,j}T^{22}_{i,j}Bv_x]}{[T^{21}_{i,j}Bv_y - T^{22}_{i,j}Bu_y]} \tag{37}$$

$$v_{i,j+1} = \frac{[(\bar{u}_{i+1,j} - \bar{u}_{i,j})T^{21}_{i,j}Bu_x + (\bar{v}_{i+1,j} - \bar{v}_{i,j})T^{21}_{i,j}Bv_x - v_{i,j}C_1(T^{21}_{i,j}T^{21}_{i,j} + T^{22}_{i,j}T^{22}_{i,j}) - 2u_{i,j}T^{21}_{i,j}Bu_y]}{[T^{22}_{i,j}Bu_y - T^{22}_{i,j}Bv_y]} \tag{38}$$

When the shear–stress balance and normal stress balance are satisfied, the velocities at the imaginary nodes have the following expressions:

$$u_{i,j+1} = u_{i,j} + \frac{\left[(\bar{u}_{i+1,j} - \bar{u}_{i,j})(Av_yBu_x - Au_xBv_y) + (\bar{v}_{i+1j} - \bar{v}_{i,j})(Av_yBv_x - Av_xBv_y) + Bv_y\left[p + \frac{\sigma}{\bar{\bar{R}}}\right]\right]}{[Au_yBv_y - Av_yBu_y]} \tag{39}$$

$$v_{i,j+1} = v_{i,j} + \frac{\left[(\bar{u}_{i+1,j} - \bar{u}_{i,j})(Av_xBu_y - Au_yBu_x) + (\bar{v}_{i+1j} - \bar{v}_{i,j})(Av_xBu_y - Au_yBv_x) + Bu_y\left[p + \frac{\sigma}{\bar{\bar{R}}}\right]\right]}{[Av_yBu_y - Au_yBv_y]} \tag{40}$$

the kinematic condition is then used to update the free surface boundary.

For the particular geometry presented here, the mean curvature is given by

$$\frac{1}{\bar{\bar{R}}} = \frac{h_{xx}}{(1 + h_x^2)^{3/2}} \tag{41}$$

where h is the distance from the mid-plane of symmetry and the subscript x denotes differentiation with respect to x as shown in Figure 1.

Following Ryskin and Leal [16], Pacheco and Peck [11] obtained the steady shape of a free surface in their solution scheme via an interative process in which the imbalance between the total normal stress and pressure for a given estimated shape of the interface is used to obtain an improved shape for the next iteration, i.e., a shape for which condition (23) is nearly satisfied. An alternative for improving the boundary profile is to consider the local excess of total normal stress

$$\Pi = p - \left[(\bar{u}_{i+1,j} - \bar{u}_{i,j}) A u_x + (\bar{v}_{i+1,j} - \bar{v}_{i,j}) A v_x + (v_{i+1,j} - v_{i,j}) A v_y + (u_{i,j+1} - u_{i,j}) A u_y + \left(\sigma \frac{1}{\bar{R}} \right) \right] \tag{42}$$

which produces a local displacement of the surface in the direction of the force. Correcting the displacement in terms of a function $h(x)$, we can use

$$h(x)^{n+1} = h(x)^n + \omega \Pi^n \tag{43}$$

to update the values for x and y, which are used as the necessary boundary conditions to determine the mapping. The relaxation parameter ω has to be found by numerical experiment. The displacement of the boundary points must occur in a direction that reduces the violation of global conservation of mass in the current flow field.

The first solution method examined in this work uses the kinematic condition to update the boundary of the free surface. After the flow field has been calculated, a new free surface is determined from the kinematic condition. In differential form, it is

$$\frac{\mathrm{d}h^{n+1}}{\mathrm{d}x} = \frac{\hat{v}^{n+1}}{\hat{u}^{n+1}} \tag{44}$$

with boundary conditions $h^{n+1} = 1$ at $x = 0$.

Kinematic iteration simply means that after a flow field has been calculated, a new free surface shape is determined from the kinematic condition. Solving the governing equations (11) and (12) with boundary conditions (3) and (4) requires us to specify an initial guess of the position of the free surface. At this point, we have not demanded in the boundary conditions that there be zero velocity flux across the free surface, we iterate in the following way: Let $h(x)^n$ be the proposed free surface, then the updated free surface $h(x)^{n+1}$, where

$$h(x_j)^{n+1} = h(x_{j-1})^{n+1} + \int_{x_{j-1}}^{x_j} \frac{\hat{v}^{n+1}}{\hat{u}^{n+1}} \mathrm{d}x \tag{45}$$

with $h(x)^{n+1} = h_{\mathrm{in}}$. Here $\hat{u}^{n+1}$ and $\hat{v}^{n+1}$ are the velocities on $h(x)^n$ being determined from the solution of the governing equations at the nth iteration.

The use of the normal stress iteration scheme is an alternative way to calculate new meniscus locations $h(x)^{n+1}$ after the $n+1$th approximation to the flow has been calculated for flows with high surface tension.

New profiles are generated from the discretized form of

$$\frac{\mathrm{d}}{\mathrm{d}x} \left[\frac{h_x}{(1+h_x^2)^{1/2}} \right] = \frac{1}{\sigma} \left[(\bar{u}_{i+1,j} - \bar{u}_{i,j}) A u_x + (\bar{v}_{i+1,j} - \bar{v}_{i,j}) A v_x + (v_{i,j+1} - v_{i,j}) A v_y + (u_{i,j+1} - u_{i,j}) A u_y \right] - \frac{1}{\sigma} p \tag{46}$$

The boundary conditions for Equation (46) are

$$h(0) = 1 \tag{47}$$

and

$$h_x(L_2) = 0 \tag{48}$$

Requiring in the kinemtic case that $v = 0$ at $x = L^2$ in the flow field calculation ensures that $h_x(L_2) = 0$ if Equation (44) is satisfied. We can integrate Equation (46) to obtain h_x on the free surface starting from the end of the jet L_2 (Figure 1). Once h_x is obtained, we can integrate h_x starting from the separation point at $x = 0$ to determine the position of the free surface.

5. NUMERICAL PROCEDURE

We solve the governing equations that describe the fluid motion in the transformed plane by the finite difference method. The step-by-step procedure is as follows:

1. Choose some initial shape of the free surface.
2. Apply the appropriate boundary conditions for the free surface by iterating on either Equations (37) and (38) in step 3 or Equations (39) and (40) in step 4 to obtain convergent velocities at the free surface.
3. Normal stress iteration:
   - compute the normal stress and check if it is zero; if Equation (23) is not satisfied, modify the interface shape so as to reduce the imbalance between the pressure and the viscous stress.
4. Kinematic condition:
   - calculate the amount of mass that is crossing the free surface; if the amount of mass that is crossing the boundary is greater than a prefixed tolerance, update the free surface using Equation (45).
5. Solve for the flow field using the fractional step method.
6. Return to step 2 until steady state is reached.
7. Compute the approximate boundary fitted co-ordinate system taking the new position of the free surface as boundary conditions.
8. Return to step 2 and repeat until all equations and boundary conditions are satisfied up to a prescribed accuracy.

Convergence was achieved when the relative change in field values between the ith iteration and the $i + k$th iteration reached a prescribed tolerance ($k \geq 1$). The stopping criteria for all cases was set to 1.0×10^{-4}.

6. RESULTS AND DISCUSSION

The results reported here are restricted to $Re \leq 100$ and $Ca \leq 1000$. In order to have a solution independent of the length we have chosen the values of L_1 and L_2 such that the change in the length will not affect the solution. We found that $L_1 = 4$ was adequate for the ranges of Re and Ca numbers presented here; whereas $L_2 = 25$ was adequate for $Re < 20$, $L_2 = 105$ for $Re = 100$. Also, the number of grid points was selected in a way that the swell ratio did not change when increasing the number of grid points. The grid size was reduced from a coarse to a finer mesh, so that the swell ratio beyond this mesh size remained unaffected by any change in the grid structure. The results are presented in Table I for $Ca = 1000$ and two different values of Re. The corresponding computational cost increases substantially as the number of discrete mesh points increases; therefore, for all calculations reported here, the number of grid points ranged from 225×25 to 525×25.

In order to check the computer code we have considered first a particular case of the two-dimensional jet when the fluid has infinite surface tension ($Ca = 0$) and zero Reynolds number. The velocities at the slip plane and centerline were compared with the exact solution given by Richardson [17] as well as the pressure variation along the centerline of the flow. The predictions agreed within 2 per cent. Figure 2 shows the values of the different terms in the normal stress condition as well as the shape of the jet for $Ca = 0.01$ and $Re = 0$.

The shapes of the numerically simulated jet determined by different numerical approaches are given in Figure 3. The jet swell ratio, Co, based on the present simulation is 1.167, whereas a value of 1.19 was obtained by Ruschak [6], 1.180 by Yu and Liu [10], and 1.160 by Pacheco and Peck [15]. The pressure contour plot for the creeping Newtonian jet is shown in Figure 4. The jet reaches its final thickness at a downstream length $x = 2$.

The numerical errors for the conditions at the free surface (the amount of mass that is crossing the free surface and the imbalance of the normal stress and shear–stress) are the local residuals, which are the left-hand side of the discretized equations subtracted from the right-hand side at each grid point along the free surface.

The creeping jet swell ratio predicted by the present method is lower than the finite element method and finite difference method with streamfunction–vorticity formulation. However, the errors for the conditions at the free surface close to the die lip are lower than those reported

Table I. Effects of mesh refinement on swell ratio with $Ca = 1000$.

Grid points	Re	Co
125×25	0	17.3
225×25		16.7
525×25		16.7
1525×50		16.7
225×25	100	-10.3
425×25		-13.7
525×25		-14.2
1525×50		-14.2

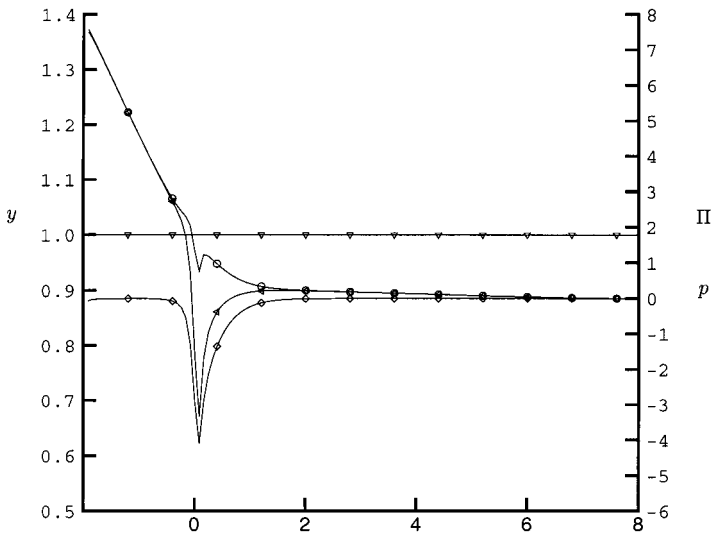

Figure 2. Components of the normal stress and residue for $Re = 0$ and $Ca = 0.01$ at the free surface. $-\triangledown-$, free surface; $-\bigcirc-$, residue Π; $-\triangleleft$-, pressure p; $-\diamondsuit-$, viscous part Π—p.

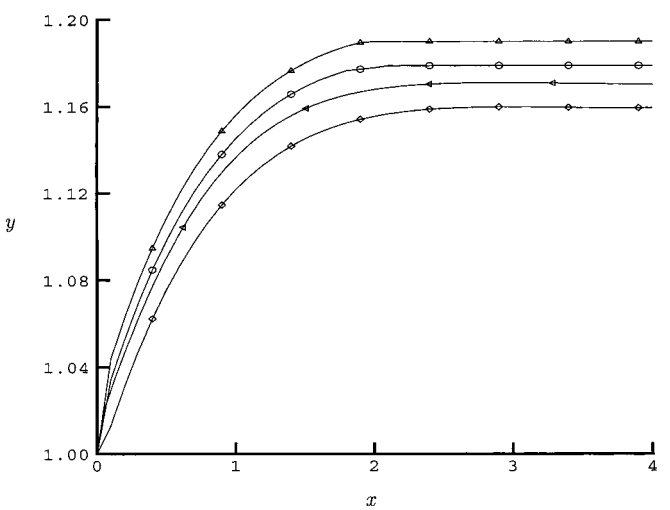

Figure 3. Comparison of the surface shapes for creeping Newtonian jet with $Ca = 1000$: $-\triangle-$ Ruschak [6]; $-\bigcirc-$ Yu and Liu [10]; $-\diamondsuit-$ normal stress condition, Pacheco and Peck [11]; $-\triangleleft-$ kinematic condition (present).

Figure 4. Pressure contours for the creeping Newtonian jet and $Ca = 100$.

by other researchers. The lack of agreement among the results reported by different researchers using different methods can be explained by the lack of accuracy in satisfying the boundary conditions at the exit of the die lip. The information propagates downstream all the way to the region of the flow considered uniform, affecting the amount of contraction or expansion of the jet flow.

Tables II, III and IV compare the numerical errors for the conditions at the free surface of this work and Liu *et al.* [18] for different values of Reynolds and Capillary numbers. In our method, the errors presented for the normal stress and shear stress conditions are of the same magnitude as those reported by Liu *et al.* [18]; however, the condition in the divergence at the separation point obtained with the method proposed here yields better results than those presented elsewhere.

The maximum error in the normal stress balance occurs at the separation point as shown in Figures 5–7 for different cases, but the residuals decay rapidly along the jet free surface and are of order 10^{-6}.

Table II. A comparison of errors on the jet surface with $Re = 0$, $Ca = 1000$.

	Liu *et al.* [18]			Present		
x	τ_{xx}	τ_{xy}	$\nabla \cdot \mathbf{u}$	τ_{xx}	τ_{xy}	$\nabla \cdot \mathbf{u}$
0.1	$4.3 \cdot 10^{14}$	$7.2 \cdot 10^{-2}$	$1.3 \cdot 10^{0}$	$8.41 \cdot 10^{-2}$	$1.86 \cdot 10^{-4}$	$1.31 \cdot 10^{-4}$
0.2	$3.8 \cdot 10^{-4}$	$-3.2 \cdot 10^{-2}$	$-5.5 \cdot 10^{-1}$	$7.78 \cdot 10^{-2}$	$-1.49 \cdot 10^{-5}$	$5.56 \cdot 10^{-5}$
0.3	$3.5 \cdot 10^{-5}$	$-4.5 \cdot 10^{-3}$	$-1.4 \cdot 10^{-1}$	$5.29 \cdot 10^{-2}$	$-3.50 \cdot 10^{-6}$	$2.45 \cdot 10^{-5}$
0.4	$5.8 \cdot 10^{-5}$	$-1.7 \cdot 10^{-3}$	$-1.0 \cdot 10^{-1}$	$3.80 \cdot 10^{-2}$	$-3.69 \cdot 10^{-6}$	$1.48 \cdot 10^{-5}$
0.5	$6.3 \cdot 10^{-5}$	$-6.4 \cdot 10^{-4}$	$-6.4 \cdot 10^{-2}$	$1.82 \cdot 10^{-2}$	$-2.56 \cdot 10^{-6}$	$3.14 \cdot 10^{-6}$
0.6	$3.2 \cdot 10^{-5}$	$-3.0 \cdot 10^{-4}$	$-4.2 \cdot 10^{-2}$	$1.25 \cdot 10^{-2}$	$-1.73 \cdot 10^{-6}$	$4.99 \cdot 10^{-7}$
0.7	$2.9 \cdot 10^{-7}$	$-1.3 \cdot 10^{-4}$	$-2.8 \cdot 10^{-2}$	$8.48 \cdot 10^{-3}$	$-1.49 \cdot 10^{-6}$	$-1.72 \cdot 10^{-6}$
0.8	$-1.0 \cdot 10^{-6}$	$-7.6 \cdot 10^{-5}$	$-2.0 \cdot 10^{-2}$	$3.74 \cdot 10^{-3}$	$-6.39 \cdot 10^{-7}$	$-3.48 \cdot 10^{-6}$
0.9	$-7.6 \cdot 10^{-6}$	$-7.0 \cdot 10^{-5}$	$-1.4 \cdot 10^{-2}$	$2.44 \cdot 10^{-3}$	$-4.31 \cdot 10^{-7}$	$-4.09 \cdot 10^{-6}$
1.0	$-2.7 \cdot 10^{-6}$	$-6.9 \cdot 10^{-5}$	$-1.0 \cdot 10^{-2}$	$1.56 \cdot 10^{-3}$	$-3.31 \cdot 10^{-7}$	$-4.51 \cdot 10^{-6}$
1.3	$2.0 \cdot 10^{-8}$	$-4.3 \cdot 10^{-5}$	$-4.2 \cdot 10^{-3}$	$2.19 \cdot 10^{-4}$	$-3.89 \cdot 10^{-8}$	$-4.57 \cdot 10^{-6}$
1.6	$-8.3 \cdot 10^{-7}$	$1.4 \cdot 10^{-5}$	$-1.4 \cdot 10^{-3}$	$1.78 \cdot 10^{-4}$	$7.55 \cdot 10^{-8}$	$-3.63 \cdot 10^{-6}$
2.0	$-1.9 \cdot 10^{-8}$	$-7.5 \cdot 10^{-6}$	$-5.0 \cdot 10^{-3}$	$-1.56 \cdot 10^{-6}$	$8.06 \cdot 10^{-8}$	$-2.34 \cdot 10^{-6}$
3.5	$-8.2 \cdot 10^{-9}$	$-4.4 \cdot 10^{-6}$	$-2.0 \cdot 10^{-5}$	$-2.24 \cdot 10^{-7}$	$9.60 \cdot 10^{-9}$	$-1.31 \cdot 10^{-6}$
7.0	$7.9 \cdot 10^{-10}$	$-8.5 \cdot 10^{-7}$	$-6.0 \cdot 10^{-5}$	$-8.56 \cdot 10^{-9}$	$-1.16 \cdot 10^{-10}$	$1.78 \cdot 10^{-9}$
9.5	$-7.3 \cdot 10^{-9}$	$-1.0 \cdot 10^{-7}$	$-6.0 \cdot 10^{-5}$	$-8.6 \cdot 10^{-9}$	$-2.26 \cdot 10^{-10}$	$2.80 \cdot 10^{-9}$

Table III. A comparison of errors on the jet surface with $Re = 1$, $Ca = 1000$.

x	Liu *et al.* [18]			Present		
	τ_{xy}	τ_{xx}	$\nabla \cdot \mathbf{u}$	τ_{xy}	τ_{xx}	$\nabla \cdot \mathbf{u}$
0.1	$8.6 \cdot 10^{-2}$	$7.1 \cdot 10^{-4}$	$1.1 \cdot 10^{0}$	$8.4 \cdot 10^{-2}$	$1.8 \cdot 10^{-4}$	$1.3 \cdot 10^{-4}$
0.2	$-3.1 \cdot 10^{-2}$	$4.8 \cdot 10^{-4}$	$-5.1 \cdot 10^{-1}$	$7.7 \cdot 10^{-2}$	$1.4 \cdot 10^{-5}$	$5.5 \cdot 10^{-5}$
0.3	$-4.6 \cdot 10^{-3}$	$1.7 \cdot 10^{-4}$	$-1.3 \cdot 10^{-1}$	$5.2 \cdot 10^{-2}$	$3.5 \cdot 10^{-6}$	$2.4 \cdot 10^{-5}$
0.4	$-1.8 \cdot 10^{-3}$	$7.3 \cdot 10^{-5}$	$-1.0 \cdot 10^{-1}$	$3.8 \cdot 10^{-2}$	$3.6 \cdot 10^{-6}$	$1.4 \cdot 10^{-5}$
0.5	$-5.9 \cdot 10^{-4}$	$5.2 \cdot 10^{-6}$	$-6.1 \cdot 10^{-2}$	$1.8 \cdot 10^{-2}$	$2.5 \cdot 10^{-6}$	$3.1 \cdot 10^{-6}$
0.6	$-2.6 \cdot 10^{-4}$	$-2.3 \cdot 10^{-5}$	$-4.0 \cdot 10^{-2}$	$1.2 \cdot 10^{-2}$	$1.7 \cdot 10^{-6}$	$4.9 \cdot 10^{-7}$
0.7	$-1.8 \cdot 10^{-4}$	$-1.5 \cdot 10^{-5}$	$-2.8 \cdot 10^{-2}$	$8.4 \cdot 10^{-3}$	$1.4 \cdot 10^{-6}$	$1.7 \cdot 10^{-6}$
0.8	$-1.3 \cdot 10^{-4}$	$-1.5 \cdot 10^{-5}$	$-1.9 \cdot 10^{-2}$	$3.7 \cdot 10^{-3}$	$6.3 \cdot 10^{-7}$	$3.4 \cdot 10^{-6}$
0.9	$-1.2 \cdot 10^{-4}$	$-6.3 \cdot 10^{-6}$	$-1.4 \cdot 10^{-2}$	$2.4 \cdot 10^{-3}$	$4.3 \cdot 10^{-7}$	$4.0 \cdot 10^{-6}$
1.0	$-1.4 \cdot 10^{-4}$	$6.7 \cdot 10^{-6}$	$-1.0 \cdot 10^{-2}$	$1.5 \cdot 10^{-3}$	$3.3 \cdot 10^{-7}$	$4.5 \cdot 10^{-6}$
2.0	$-3.2 \cdot 10^{-5}$	$1.1 \cdot 10^{-6}$	$8.6 \cdot 10^{-4}$	$2.1 \cdot 10^{-4}$	$3.8 \cdot 10^{-8}$	$4.5 \cdot 10^{-6}$
3.0	$3.0 \cdot 10^{-6}$	$-3.6 \cdot 10^{-8}$	$5.0 \cdot 10^{-4}$	$2.1 \cdot 10^{-4}$	$3.8 \cdot 10^{-8}$	$4.5 \cdot 10^{-6}$
4.0	$-3.7 \cdot 10^{-6}$	$-6.9 \cdot 10^{-9}$	$-1.1 \cdot 10^{-4}$	$2.1 \cdot 10^{-4}$	$3.8 \cdot 10^{-8}$	$4.5 \cdot 10^{-6}$
5.0	$3.0 \cdot 10^{-7}$	$3.5 \cdot 10^{-10}$	$-1.1 \cdot 10^{-4}$	$2.1 \cdot 10^{-4}$	$3.8 \cdot 10^{-8}$	$4.5 \cdot 10^{-6}$
6.0	$-6.8 \cdot 10^{-6}$	$5.1 \cdot 10^{-10}$	$-5.9 \cdot 10^{-5}$	$2.1 \cdot 10^{-4}$	$3.8 \cdot 10^{-8}$	$4.5 \cdot 10^{-6}$
7.0	$-2.2 \cdot 10^{-6}$	$6.0 \cdot 10^{-10}$	$-3.0 \cdot 10^{-5}$	$2.1 \cdot 10^{-4}$	$3.8 \cdot 10^{-8}$	$4.5 \cdot 10^{-6}$
8.0	$1.4 \cdot 10^{-5}$	$-9.5 \cdot 10^{-10}$	$-2.7 \cdot 10^{-5}$	$2.1 \cdot 10^{-4}$	$3.8 \cdot 10^{-8}$	$4.5 \cdot 10^{-6}$
9.0	$-4.4 \cdot 10^{-6}$	$-5.0 \cdot 10^{-10}$	$-7.0 \cdot 10^{-6}$	$1.7 \cdot 10^{-4}$	$7.5 \cdot 10^{-8}$	$3.6 \cdot 10^{-6}$
10.0	$-3.8 \cdot 10^{-6}$	$-1.2 \cdot 10^{-8}$	$-1.7 \cdot 10^{-5}$	$-8.5 \cdot 10^{-9}$	$1.1 \cdot 10^{-10}$	$1.7 \cdot 10^{-9}$

The vector plot of the velocities for $Re = 100$ and $Ca = 1000$ is presented in Figure 8. It is clear that the velocity downstream is not uniform at $L_2 = 14$; however, we can use the radiation boundary condition for the velocities in the spanwise direction without requiring to increase the length of the jet. We have experimented with both types of boundary conditions and the results are almost identical. Table V shows the jet swell for values of the capillary number between 0 and 1000 when the Reynolds number is 0. The jet expands monotonically at low Re. The predicted free surface profiles for different Ca numbers are presented in Figure 9. The results show how the jet expands monotonically at low Re as Ca increases. The effect of Re on the shape of the free surface is shown in Figure 10. The jet contracts at high Re. Table VI presents the jet swells for Reynolds numbers up to 100 when surface tension is negligible.

In our computation scheme, the mass imbalance must be minimized at each time step in order to relocate the free surface boundary to its final position in the steady state solution. Therefore, in applying the kinematic scheme we set the volume flux leaving the free surface boundary to be within 1 per cent of the total volume flux leaving the die lip. This condition restricts the movement of the free surface to low values, causing slow convergence. In addition, the method uses a pseudo-transient approach to reach steady state.

Table IV. A comparison of errors on the jet surface with $Re = 100$, $Ca = 1000$.

x	Liu *et al.* [18]			Present		
	τ_{xy}	τ_{xx}	$\nabla \cdot \mathbf{u}$	τ_{xy}	τ_{xx}	$\nabla \cdot \mathbf{u}$
0.1	$8.7 \cdot 10^{-2}$	$1.5 \cdot 10^{-2}$	$5.2 \cdot 10^{-1}$	$2.1 \cdot 10^{-5}$	$4.5 \cdot 10^{-4}$	$8.1 \cdot 10^{-5}$
0.2	$-8.0 \cdot 10^{-2}$	$1.7 \cdot 10^{-2}$	$-1.6 \cdot 10^{-1}$	$2.3 \cdot 10^{-5}$	$2.3 \cdot 10^{-4}$	$3.9 \cdot 10^{-5}$
0.3	$-6.6 \cdot 10^{-2}$	$-2.7 \cdot 10^{-3}$	$-8.3 \cdot 10^{-2}$	$2.2 \cdot 10^{-5}$	$1.4 \cdot 10^{-4}$	$1.5 \cdot 10^{-5}$
0.4	$-4.4 \cdot 10^{-2}$	$-1.3 \cdot 10^{-2}$	$-1.0 \cdot 10^{-1}$	$1.8 \cdot 10^{-5}$	$8.6 \cdot 10^{-5}$	$9.5 \cdot 10^{-6}$
0.5	$-2.0 \cdot 10^{-2}$	$-1.4 \cdot 10^{-2}$	$-9.2 \cdot 10^{-1}$	$1.6 \cdot 10^{-5}$	$1.1 \cdot 10^{-4}$	$1.6 \cdot 10^{-5}$
0.6	$8.0 \cdot 10^{-3}$	$-8.7 \cdot 10^{-3}$	$-5.2 \cdot 10^{-2}$	$1.5 \cdot 10^{-5}$	$7.3 \cdot 10^{-5}$	$8.1 \cdot 10^{-6}$
0.7	$3.4 \cdot 10^{-2}$	$-3.8 \cdot 10^{-4}$	$1.3 \cdot 10^{-2}$	$1.3 \cdot 10^{-5}$	$9.3 \cdot 10^{-5}$	$1.2 \cdot 10^{-5}$
0.8	$5.0 \cdot 10^{-2}$	$7.0 \cdot 10^{-3}$	$8.5 \cdot 10^{-2}$	$1.2 \cdot 10^{-5}$	$6.6 \cdot 10^{-5}$	$7.9 \cdot 10^{-6}$
0.9	$4.5 \cdot 10^{-2}$	$1.0 \cdot 10^{-2}$	$1.3 \cdot 10^{-1}$	$1.0 \cdot 10^{-5}$	$7.7 \cdot 10^{-5}$	$1.0 \cdot 10^{-5}$
1.0	$3.0 \cdot 10^{-2}$	$1.0 \cdot 10^{-2}$	$1.5 \cdot 10^{-1}$	$9.8 \cdot 10^{-6}$	$6.4 \cdot 10^{-5}$	$8.4 \cdot 10^{-6}$
2.0	$1.2 \cdot 10^{-2}$	$2.1 \cdot 10^{-5}$	$6.9 \cdot 10^{-2}$	$3.1 \cdot 10^{-6}$	$6.0 \cdot 10^{-5}$	$1.0 \cdot 10^{-6}$
3.0	$-3.0 \cdot 10^{-3}$	$1.1 \cdot 10^{-4}$	$2.6 \cdot 10^{-3}$	$1.3 \cdot 10^{-6}$	$1.6 \cdot 10^{-5}$	$2.6 \cdot 10^{-6}$
4.0	$2.7 \cdot 10^{-3}$	$-5.9 \cdot 10^{-5}$	$-1.4 \cdot 10^{-1}$	$6.2 \cdot 10^{-7}$	$4.9 \cdot 10^{-5}$	$8.9 \cdot 10^{-5}$
5.0	$-4.8 \cdot 10^{-3}$	$8.3 \cdot 10^{-5}$	$-9.7 \cdot 10^{-2}$	$3.2 \cdot 10^{-7}$	$4.0 \cdot 10^{-5}$	$7.5 \cdot 10^{-6}$
6.0	$1.0 \cdot 10^{-2}$	$2.2 \cdot 10^{-4}$	$-2.6 \cdot 10^{-1}$	$1.9 \cdot 10^{-7}$	$1.6 \cdot 10^{-5}$	$3.5 \cdot 10^{-6}$
7.0	$-7.8 \cdot 10^{-3}$	$-2.0 \cdot 10^{-4}$	$-1.9 \cdot 10^{-1}$	$1.2 \cdot 10^{-7}$	$1.1 \cdot 10^{-6}$	$9.2 \cdot 10^{-5}$
8.0	$1.6 \cdot 10^{-2}$	$-4.0 \cdot 10^{-5}$	$7.4 \cdot 10^{-2}$	$8.0 \cdot 10^{-7}$	$1.4 \cdot 10^{-5}$	$2.9 \cdot 10^{-6}$
9.0	$-2.9 \cdot 10^{-2}$	$-3.0 \cdot 10^{-4}$	$-1.6 \cdot 10^{-4}$	$5.0 \cdot 10^{-8}$	$3.0 \cdot 10^{-5}$	$5.6 \cdot 10^{-6}$
10.0	$1.5 \cdot 10^{-2}$	$9.6 \cdot 10^{-5}$	$2.2 \cdot 10^{-2}$	$3.7 \cdot 10^{-8}$	$-3.0 \cdot 10^{-6}$	$1.6 \cdot 10^{-7}$

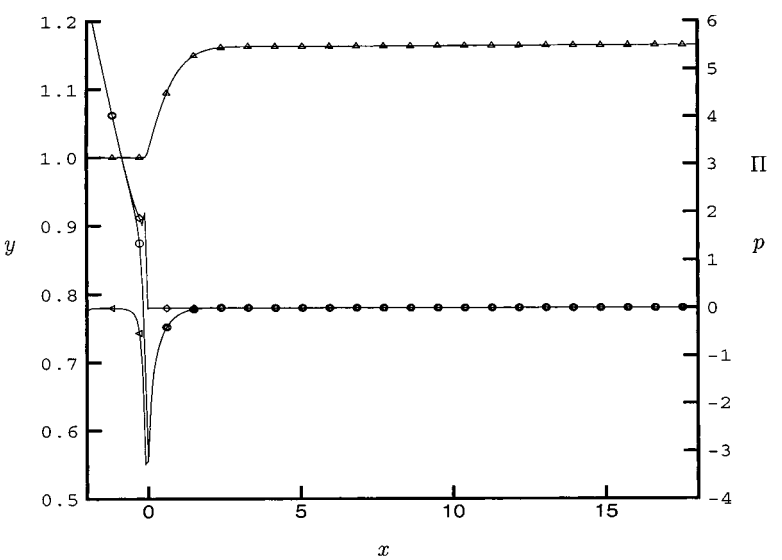

Figure 5. Components of the normal stress and residue for $Re = 0$ and $Ca = 1000$ at the free surface. $-\triangle-$, free surface profile; $-\diamond-$, residue Π; $-\circ-$, pressure p; $-\triangledown-$, viscous part Π—p.

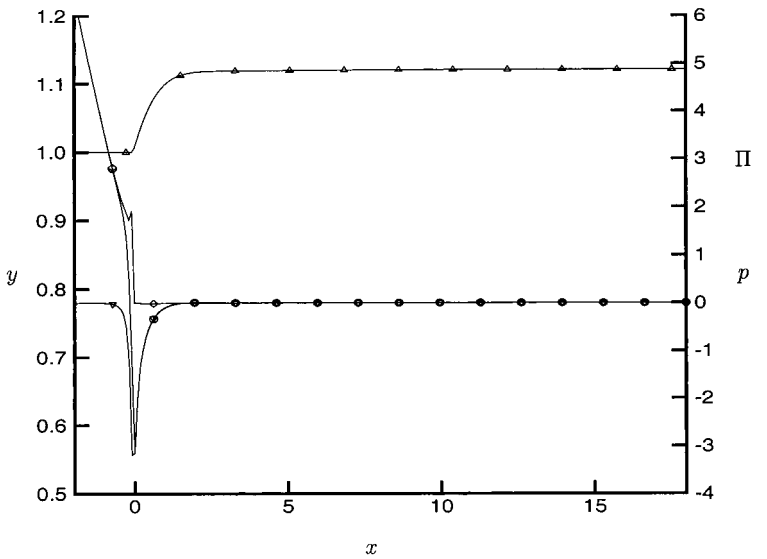

Figure 6. Components of the normal stress and residue for $Re = 0$ and $Ca = 1$ at the free surface. $-\triangle-$, free surface profile; $-\diamond-$, residue Π; $-\bigcirc-$, pressure p; $-\triangledown-$, viscous part Π—p.

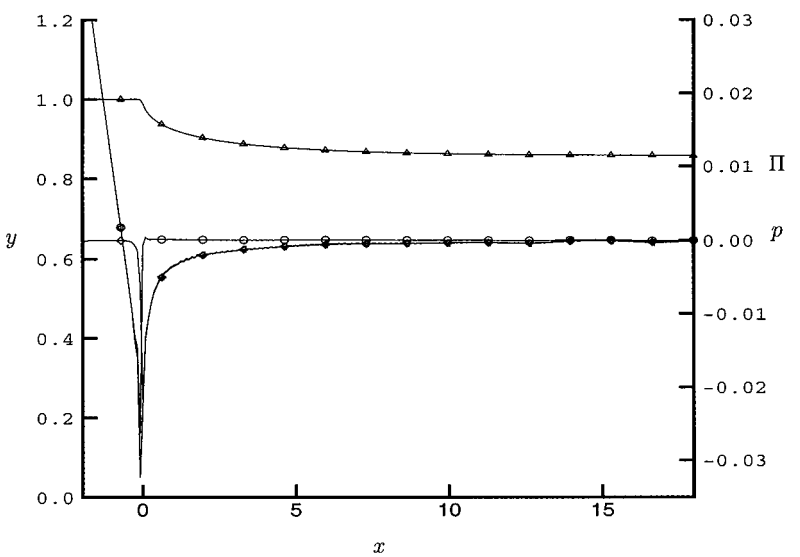

Figure 7. Components of the normal stress and residue for $Re = 100$ and $Ca = 1000$ at the free surface. $-\triangle-$, free surface profile; $-\bigcirc-$, residue Π; $-\diamond-$, pressure p, $-\triangledown-$, viscous part Π—p.

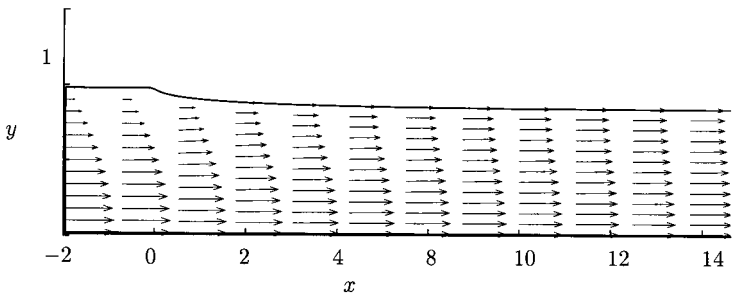

Figure 8. Vector plot of the jet flow for $Re = 100$ and $Ca = 1000$.

Table V. Percentage swell at $Re = 0$.

Ca	1000	1	0.01	0
Co	16.7	12.4	0.03	0

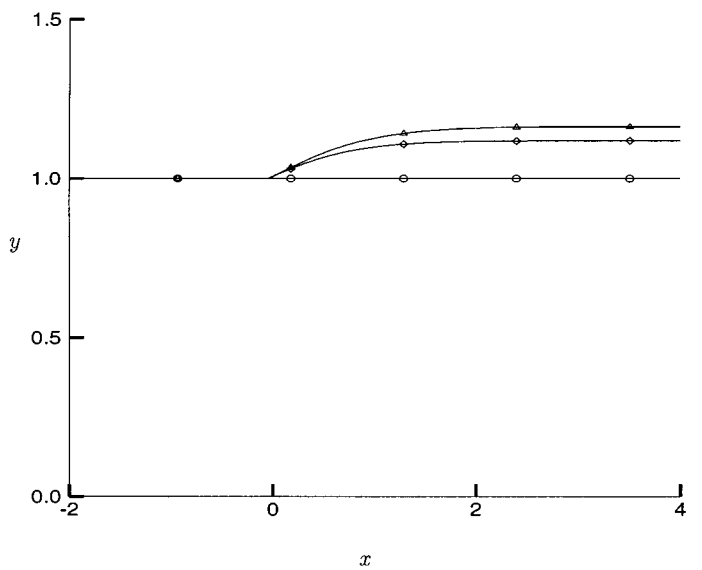

Figure 9. Effect of capillary number for $Re = 0$ on the free surface profiles. Profile $-\triangle-$, $Ca = 1000$; $-\diamond-$, $Ca = 1$; $-\bigcirc-$, $Ca = 0.01$.

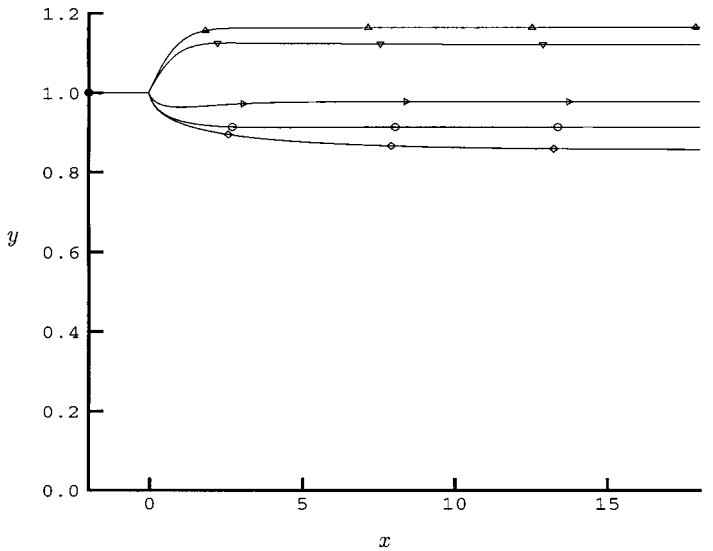

Figure 10. Effect of Reynolds number for $Ca = 1000$ on the free surface profiles. Profiles $-\triangle-$, $Re = 0$; $-\triangledown-$, $Re = 1$; $-\triangleright-$, $Re = 10$; $-\bigcirc-$, $Re = 20$; $-\diamondsuit-$, $Re = 100$.

Table VI. Percentage swell at $Ca = 1000$.

Re	0.0	1.0	10.0	20.0	100.0
Co	16.7	12.0	−2.2	−8.54	−14.2

7. CONCLUSIONS

We have developed a finite difference technique to calculate free surface flows for high and low capillary numbers and Reynolds numbers up to 100. The mathematical problem is formulated in primitive variables and solved using the fractional step method for non-staggered grids adapted from Zang *et al.* [12]. The numerical solutions for all test cases compare well with other published results. The numerical method accommodates non-orthogonal grids. Accurate predictions of the Newtonian jet problem were obtained for different values of *Re* and *Ca*. To the author's knowledge this is the first solution of the jet swell problem using finite differences with grid transformation and primitive variables and using both kinematic and normal stress schemes to locate the surface boundary. Future refinements to solve the pressure-Poisson equation are needed to improve the speed and precision of the results. A promising new technique has been developed for simulating an important class of flow problems.

ACKNOWLEDGMENTS

The author would like to thank Dr Kyle Squires for helpful discussions on this work and Mr Bruce Tachoir for access to computer facilities.

APPENDIX A. NOMENCLATURE

Au_x, Av_x	specified constants
Au_y, Av_x	specified constants
Bu_x, Bv_x	specified constants
Bu_y, Bv_y	specified constants
Ca	Capillary number
C_j	specified constants
Co	swell ratio
G^{mn}	mesh skewness tensor
g	gravitational acceleration
h	height measured from the symmetry plane
i	iteration level
J	Jacobian
k	positive integer
L	characteristic length
L_1	length of the downstream region
L_2	length of the upstream region
n_i	vector normal to the free surface
p	pressure
p_a	atmospheric pressure
R_1, R_2	radii of curvature
$\bar{R}$	average radius of curvature
Re	Reynolds number
t	time
T^{ij}	Cartesian tensor times the Jacobian
U	characteristic velocity
U, V	volume flux in the ξ, η co-ordinates
U_m	volume flux
u_i, (u, v)	Cartesian velocity at the cell
$\hat{u}_i$, $(\hat{u}, \hat{v})$	Cartesian velocity defined at the center-face of the cell
$\bar{u}_i$, $(\bar{u}, \bar{v})$	Cartesian velocity defined at the corner of the cell
x_i, (x, y)	Cartesian co-ordinates
W	Weber number

Greek letters

δ_{ij}	Kronecker delta
κ	curvature
μ	dynamic viscosity
ν	kinematic viscosity
ρ	fluid density
σ	surface tension
τ_{ij}	stress tensor
τ_{xx}	normal stress
τ_{xy}	shear stress
ω	relaxation parameter
ξ_m, (ξ, η)	curvilinear co-ordinates
Γ	domain boundary
Γ_{in}	domain boundary (inlet)
Γ_{out}	domain boundary (outlet)
Γ_{s}	domain boundary (symmetry)
Γ_0	domain boundary (no-slip)
Γ_σ	domain boundary (traction)
Π	excess in local normal stress
Ω	domain

Subscripts and superscripts

i, j	indices for the Cartesian co-ordinates or vector quantities
in	inlet
m, n	indices for the curvilinear co-ordinates
n	index of time step
out	outlet
s	symmetry
x	x-direction
	first derivative in the x-direction
xx	second derivative in the x-direction
y	y-direction
0	no-slip boundary condition
σ	traction boundary condition

REFERENCES

1. Ho LW, Patera AT. A Legendre spectral element method for simulation of unsteady incompressible viscous free-surface flows. *Computers in Applied Mechanics and Engineering* 1990; **80**: 355–366.
2. Lin SP. *Waves on Fluid Interfaces*. Academic Press: New York, 1983.

3. Krantz WB, Goren SL. Stability of thin liquid films flowing down a plane. *Industrial Engineering and Chemistry Fundamentals* 1971; **10**: 91–100.
4. Kang F, Chen KP. Nonlinear elastic instability of gravity-driven flow of a thin viscoelastic film down an inclined plane. *Journal of Non-Newtonian Fluid Mechanics* 1995; **57**: 243–252.
5. Tillet JPK. On the laminar flow of a free jet of liquid at high Reynolds numbers. *Journal of Fluid Mechanics* 1968; **32**: 273–292.
6. Ruschak KJ. A method for incorporating free boundaries with surface tension in finite-element fluid-flow simulators. *International Journal for Numerical Methods in Engineering* 1980; **15**: 639–648.
7. Nickell RE, Tanner RI, Caswell B. The solution of viscous incompressible jet and free surface-flows using finite-element methods. *Journal of Fluid Mechanics* 1974; **65**: 189–206.
8. Ho L-W, Rønquist EM. Spectral element solution of steady incompressible viscous free-surface flows. *Finite Elements with Analytical Design* 1994; **16**: 207–227.
9. Han CT, Tasi CC, Yu SH, Liu TJ. A finite difference technique for solving the Newtonian jet swell problem. *International Journal for Numerical Methods in Fluids* 1992; **15**: 773–789.
10. Yu SH, Liu TJ. An improved finite difference scheme for a Newtonian jet swell problem. *International Journal for Numerical Methods in Fluids* 1992; **14**: 495–501.
11. Pacheco JR, Peck RE. Non-staggered grid boundary-fitted coordinate method for free surface flows. *Numerical Heat Transfer Part B* 2000; **37**: 267–291.
12. Zang Y, Street RI, Kossef JF. A non-staggered grid, fractional step method for time dependent incompressible Navier–Stokes equations in curvilinear coordinates. *Journal of Computational Physics* 1994; **114**: 18–33.
13. Thompson JF, Thames FC, Mastin CM. Boundary-fitted coordinate systems for numerical solution of partial differential equations—a review. *Journal of Computational Physics* 1982; **47**: 1–107.
14. Steger JL, Sorenson RL. Automatic mesh-point clustering near a boundary in grid generation with elliptic partial differential equations. *Journal of Computational Physics* 1979; **33**: 405–410.
15. Pacheco JR, Peck RE. Non-staggered grid boundary-fitted coordinate method for free surface flows. In *1st International Symposium on Computational Technologies for Fluid/Thermal/Chemical Systems with Industrial Applications*, San Diego, CA, vol. 337-1, Kudriavtsev VV, Cheng W (eds), 1998; 49–59.
16. Ryskin G, Leal LG. Numerical solution of free-boundary problems in fluid mechanics. Part 1. The finite-difference technique. *Journal of Fluid Mechanics* 1984; **148**: 1–17.
17. Richardson S. A 'stick-slip' problem related to the motion of a free jet with surface tension. *Proceedings of the Cambridge Philosophical Society* 1970; **67**: 477–487.
18. Liu TJ, Yu TA, Cheng SH. Finite difference solution of a Newtonian jet swell problem. *International Journal for Numerical Methods in Fluids* 1991; **12**: 125–141.

